EXPERIMENTAL MEASUREMENTS OF HYDRODYNAMIC STIFFNESS MATRICES FOR A CENTRIFUGAL PUMP IMPELLER*

D. S. Chamieh, A. J. Acosta, C. E. Brennen, T. K. Caughey, and R. Franz
California Institute of Technology
Pasadena, California 91125

ABSTRACT

The objective of the Rotor Force Test Facility at the California Institute of Technology is to artificially orbit the center of rotation of an impeller enclosed within a volute over a range of frequencies from zero to synchronous and to measure the resulting forces on the impeller. This paper reports preliminary data from the first stage experiments in which the shaft is orbited at low frequency. Steady volute forces along with stiffness matrices due to the change in position of the rotor center are measured. Static pressure taps around the volute are used to obtain volute pressure distributions for various fixed positions of the impeller center and for various flow rates. Static pressure forces are calculated from these pressure distributions allowing a more complete analysis of the components of the impeller forces. Comparison is made with various existing theoretical and experimental results.

INTRODUCTION

It has become evident in the last few years that the main flow through a pump or compressor can contribute to the rotor dynamic inertia, damping and stiffness matrices of the machine in a significant way (ref.1, 2). Consequently in many applications an accurate rotor dynamic analysis of a turbomachine may require inclusion of the components of these matrices resulting from the flow through the impeller as well as the contributions from seals and bearings. In the past the hydrodynamic forces on a radial impeller enclosed in a volute have been primarily studied experimentally and many of the earlier references are based on the semi-empirical relation introduced by Stepanoff (Ref.3). Other experimental papers followed in the same spirit namely those of Domm and Hergt (Ref.4), Agostinelli et al (Ref.5) and Iversen et al (Ref.6). Later as a first step towards studying the whirling problem, Hergt and Krieger (Ref.7) measured radial forces at various eccentricities of the impeller.

Theoretical studies directed toward evaluation of the impeller forces include the work of Domm and Hergt (Ref.4) who modelled the impeller by a source vortex placed within the volute. Their analysis demonstrated the existence of a lateral force on the impeller even in the absence of an orbiting motion of the shaft. Colding-Jorgensen (Ref.8) extended the work of Domm and Hergt (Ref.4) by imposing an orbiting motion on the source/vortex model of the impeller. His results are discussed below. Other more complex methods have also been developed. The actuator disk model, suggested by Chamieh and Acosta (Refs. 9, 10) was used to obtain inertial terms that do not arise in the source-vortex model. More recently both Imaichi, Tsujimoto and Yoshida (Ref. 11) and Shoji and Ohashi (Ref.12) represent the impeller wakes by a finite number of rotating vortex sheets. Imaichi et al (Ref.11) solved the unsteady problem of a fixed impeller inside a volute and Ohashi et al (Ref.12) solved the unbounded whirling problem. However neither were able to formulate the more complex problem of an orbiting impeller enclosed within a volute.

---

*This work is supported by NASA George Marshall Space Flight Ctr.,Contract NAS 8-33108.

NOMENCLATURE

A_2	Impeller discharge area = $2\pi R_2 b_2$
b_2	Impeller discharge width
C_P	Pressure coefficient, $(p - p_{T2})/\frac{1}{2}\rho U_2^2$
$\underline{e}$	Instantaneous vector displacement of the external balance flexure system
$\{F_o\}$	Average volute force on impeller (vector)
$\{F_o^*\}$	Non-dimensional average volute force on impeller (vector) = $\{F_o\}/\frac{1}{2}\rho A_2 U_2^2$
F_x^*, F_y^*	Components of $\{F_o^*\}$ in X,Y directions (see Fig.4)
$\underline{F_i}$, $\{F_i\}$	Instantaneous hydrodynamic force on impeller (vector)
$\{F_\Omega\}$	Fundamental harmonic component of $\{F_i\}$
$\{K_s\}$	Stiffness matrix for external balance
$\{K_{ij}\}$	Hydrodynamic force matrix for volute/impeller
$\{K_{ij}^*\}$	Non-dimensional hydrodynamic force matrix
N,ω	Main shaft speed (rpm and radian/sec)
p	Static pressure measurement in volute
p_{T2}	Discharge total pressure
Q	Volume flow rate
R_2	Impeller discharge radius
U_2	Impeller tip speed
t	Time
X,Y	Cartesian coordinates (Fig.4)
$\underline{\delta}$, $\{\delta\}$	Instantaneous position of impeller center (vector, Fig.4)
$\{\delta_o\}$	Mean position of impeller center
$\{\delta_\Omega\}$	Fundamental harmonic component of $\{\delta\}$
$\underline{\varepsilon}$, $\{\varepsilon\}$	Imposed eccentricity of impeller ($\lvert\varepsilon\rvert$ = 1.26mm).
λ	Logarithmic spiral angle of volute
φ	Flow coefficient, = Q/A_2U_2

ψ	Head coefficient = Total pressure rise across pump/ρU_2^2
ρ	Density of water
Ω	Radian frequency of whirl motion
θ	Angular position measured from the tongue (Fig.4)
ω	Radian frequency of impeller rotation

ROTOR FORCE TEST FACILITY

In an earlier paper (Ref.13) the facility was described in detail. We will merely repeat that the objective of the facility is to impose known orbiting motions of radian frequency Ω on the basic rotary motion of a number of typical centrifugal pump impellers (radian frequency, ω, shaft speed, N). Two force balances are incorporated: (a) a simple balance external to the bearings and seals for scoping experiments and the measurement of steady volute asymmetry forces and stiffness matrices at zero whirl frequency ($\Omega = 0$) and (b) an internal balance upon which the impeller is directly mounted for measurements at non-zero whirl frequencies (see Figs. 1, 2 and Ref.13).

This paper reports measurements using the external balance and a 16.2cm diameter five-bladed Byron-Jackson centrifugal impeller (designated Impeller X) with a specific speed of 0.57. A matching logarithmic spiral volute (Volute A) with a spiral angle of 36° was employed with this impeller (other impeller/volute combinations will be tested shortly). The volute was designed in accordance with the assumption of Ref. 3. During the measurements face seals on both sides of the impeller were backed off to prevent interference with the force measurements. Various face seal clearances were investigated. Figure 5 presents the performance characteristic for two seal clearances.

The external balance, consisting of three aluminum flexures (see Figs. 1, 2 and 4) was used with the entire impeller/eccentric drive system floating on soft spring supports attached to the ceiling. Three stainless steel flexures parallel with the shaft maintained the alignment in this configuration. A small D.C. motor was also mounted on the floating assembly to produce a shaft orbit speed of 3 rpm. The purpose of this was to allow continuous sampling of the forces at all locations of the shaft around a circular orbit with a radius of 1.26mm. By comparison with the forces at certain fixed locations it was determined that the dynamic effects of this 3 rpm orbit speed were negligible.

Two of the strain-gaged flexures are mounted horizontally (Figs.2 and 4) for measurement of horizontal force and torque; the other measures the vertical force. Calibrations were performed by known forces applied by systems of wires, pulleys and weights. The linearity of the calibrations was within 1% over the entire range of calibration (-20 to +20kg) and the interactions were less than 1%.

Signal processing was accomplished by means of an eight channel digital signal processor which was phase locked to an optical encoder attached to the shaft of the 3 rpm motor. In this way each of the 8 channels of data (three flexures plus pressure transducers, flow rates, etc) are sampled at 32 equally spaced positions of each rotation of the eccentricity. Furthermore this sampling was continued for 15 or more rotations in order to obtain averages of the forces for each of the 32 geometric positions.

The flexure signals were also recorded on magnetic tape and processed through a digital spectrum analyser to investigate their content. A major peak was observed at the 3 rpm whirl frequency. Much smaller peaks were observed at higher harmonics of this whirl frequency. The largest observed magnitude of the second harmonic was less than 10% of the fundamental indicating that the impeller forces at the small eccentricity employed here vary quite sinusoidally around the circular eccentric orbit. In other words the forces vary linearly with cartesian displacements X and Y and this variation can be accurately represented by a stiffness matrix. In addition to these low frequency components the spectral analysis also showed peaks at the shaft frequency and the higher blade passage frequencies. These represent dynamic forces which are not accurately measured by the external balance and will be the subject of a later paper based on the internal balance measurements.

The geometry and notation of the impeller shaft location, external balance flexures and volute position are shown in Figure 4 (viewed from the pump inlet).

CALCULATION OF IMPELLER VOLUTE FORCES AND STIFFNESS MATRICES

The flexure system, though quite stiff, has some deflection due to the hydrodynamic forces on the impeller; indeed this deflection is monitored by the external balance elements. One consequence of this is that the actual position of the shaft center is a combination of the 1.26mm eccentricity plus the deflection of the flexure system. All of the data on the impeller forces and stiffness matrices were corrected for this effect in the following way (see Fig.4). If $\{\varepsilon\}$ is the instantaneous shaft center due to the imposed eccentricity of 1.26mm and $[K_s]$ is the stiffness matrix of the flexure system (measured by loading under conditions of no motion) then the actual position of the shaft (see Fig.4) is

$$\{\delta\} = \{\varepsilon\} + \{e\} \; ; \; \{e\} = [K_s]^{-1}\{F_i\} \tag{1}$$

where $\{F_i\}$ is the total force acting on the floating assembly due to the Ω and ω motions. Tare forces were found to be negligible so that, with proper zeroing of the balance, the forces, $\{F_i\}$, are entirely hydrodynamic (see the no-impeller results of Figure 9 for confirmation).

Fourier decomposition of the data yielded average hydrodynamic forces $\underline{F}_o$ associated with the mean position of the shaft center and first harmonics, $\{F_\Omega\}$ and $\{\delta_\Omega\}$ at the orbit frequency, Ω (3 rpm). Then the hydrodynamic force matrix, $[K_{ij}]$ is defined as

$$\{F_\Omega\} = [K_{ij}]\{\delta_\Omega\} \tag{2}$$

where $\{\delta_\Omega\}$ is the fundamental of $\{\varepsilon + [K_s]^{-1}\{F_i\}\}$ and therefore $[K_{ij}]$ can be calculated since ε, $[K_s]^{-1}$ and $\{F_\Omega\}$ are all known. In the present experiments the correction $[K_s]^{-1}\{F_\Omega\}$ could be as large as 10% of δ_Ω.

The forces and force matrices are presented in non-dimensional form using the normalizing factors defined in the nomenclature.

ADDITIONAL MEASUREMENTS

Two types of additional measurements were performed in order to investigate the source of the impeller forces and stiffness matrices. Firstly, measurements of these quantities were also obtained (i) with different seal clearances (ii) at zero flow rate by total flow blockage exterior to the pump (iii) with the impeller inlet and/or exit blocked by sheet metal attachments (iv) with the impeller removed (v) with a dummy solid impeller having the same exterior shape. Secondly, static pressure distributions within the volute were measured by means of the static pressure taps shown in Fig.3 for four fixed positions of the eccentricity (the positions 'farthest', 'closest', 'right' and 'left' shown in Fig.4) and various flow coefficients. These pressure distributions are presented non-dimensionally using a pressure coefficient, C_p, based on the downstream total pressure and $\rho U_2^2/2$.

FORCE DATA; RESULTS AND DISCUSSION

The reduced data for the average force on Impeller X due to the Volute A when the mean position of the former is coincident with the center of the logarithmic spiral volute is presented in magnitude and direction form in Figs. 6 and 7 and in terms of its cartesian components in Fig.8. The data presented is for seal clearances of 0.14mm. However quite similar results were obtained for clearances of 0.79mm even though the performance characteristic in the latter case is significantly degraded. Some results for both a forward 3 rpm sampling orbit speed $(\Omega > 0)$ and with the direction reversed $(\Omega < 0)$ are shown to confirm that this orbit speed had little effect on the results. The non-dimensionalized force data for different shaft speeds (600 rpm up to 2000 rpm) is in substantial agreement though there would appear to be a slight increase in the magnitude of the force coefficient at low flow coefficients when the speed is increased. It seems likely that this is a Reynolds number effect. From a practical viewpoint it is clear that the Volute A and the Impeller X are well matched at their design flow coefficient $\varphi = 0.092$ since the force on the impeller is virtually zero in this operating state.

Also shown in Figs. 6 and 7 are the experimental results of Agostinelli, Nobles and Mockridge (Ref.5) and Iversen, Rolling and Carlson (Ref.6) for pumps with specific speeds of 0.61 and 0.36 respectively. The former are in close agreement with the present results since the specific speed of the present Impeller X/Volute A combination is 0.57. The results of Iversen et al for a lower specific speed also appear consistent in magnitude with the present results. For clarity a fourth set of experimental results by Domm and Hergt (Ref.4) are presented in Fig.8. These results for a similar volute $(\lambda = 86.3°)$ appear to be in substantial disagreement (lower forces by a factor of 2 or 3) with the results of Fig.6; the reason for this is not clear at the present time.

Finally Fig.8 also presents the theoretical results of both Domm and Hergt (Ref. 4) and Colding-Jorgensen (Ref.8) for volutes with angles close to the 86° of the present set-up. These theories which are based on source/vortex models of the impeller also underpredict the present results by a factor of about two.

Figure 9 present the force coefficient data for a number of tests performed with the objective of assessing the source of the large forces present at conditions of no flow ($\varphi = 0$ in Figs. 6, 7, 8). All of the data of Fig.9 appears to be virtually independent of shaft speed indicating that forces are proportional to the square of the tip speed. The lack of any appreciable force in the absence of the impeller (No impeller points) confirms that these shut-off forces are hydrodynamic in origin. The data for the solid impeller, for Impeller X with the exit blocked off by a sheet of metal and for Impeller X with both the inlet and exit similarly blocked are all similar. Though data is shown for 0.14mm face seal clearances, the data for 0.79mm face seal clearances is very similar in magnitude. We conclude that this force coefficient component (about 0.04) is due to fluid frictional effects and the induced pressure gradient acting on the entire exterior surfaces of the impeller. The data with only the impeller inlet blocked is significantly higher, probably because the discharge surface (blades and gaps) has greater friction. Finally the force data for the flow blocked exterior to the pump is significantly higher still. The reason for this is not entirely clear as yet but the associated observation of substantially greater prerotation under shut-off conditions may be significant.

HYDRODYNAMIC FORCE MATRICES

Typical non-dimensional hydrodynamic force matrices, $[K^*_{ij}]$, are presented in Fig.10; these contain all the information on how the forces presented in Figs. 7, 8 and 9 vary as the position of the impeller center changes provided the change is within the linear region. The hydrodynamic stiffness matrix experienced by the shaft is $[-K_{ij}]$. The data shown in Fig. 10 is for seal clearances of 0.14mm, various impeller speeds and flow coefficients. We observe that the variation with N is consistent with that anticipated by the non-dimensionalization and that the components vary only modestly with flow coefficient, φ, for values above about 0.03. Data has also been obtained with 0.79mm seal clearances; it is qualitatively similar to that of Fig. 10 except that the magnitude of all of the components is roughly 0.5 larger for the larger clearances. The theoretical results of Colding-Jorgensen (Ref. 8) based on the source/vortex model of the impeller which are also depicted in Fig.10 exhibit substantial disagreement with the measurements. The diagonal components K^*_{xx} and K^*_{yy} are different by a factor of 3. The off-diagonal or "cross-coupling" terms are very different in magnitude and, in the case of K^*_{yx}, the experimental data do not exhibit the change of sign near the design flow coefficient.

Both the hydrodynamic forces presented in Figs. 6, 7 and 8 and the hydrodynamic force matrices in Fig.10 imply that the fluid forces will tend to excite a whirl motion of the impeller. The force matrix could be presented approximately by the form

$$[K^*_{ij}] = \begin{bmatrix} 2.0 & -0.9 \\ 0.9 & 2.0 \end{bmatrix}$$

at least over the range $0.04 < \varphi < 0.14$. It is therefore a combination of a diagonal and a skew-symmetric matrix. The former will simply reduce the structural stiffness matrix and in many cases this hydrodynamic effect will be small. The skew-symmetric or cross-coupling terms are much more important. Since K^*_{xy} and K^*_{yx} are of opposite sign their effect is to tend to destabilize the rotor. The rotordynamic consequences of such excitation will, of course, depend on the damping matrix as well (see for example Ref.14). However since K^*_{xy} and K^*_{yx} are proportional to N^2 it follows that if the damping increases more slowly with N, then there will always be a critical speed, N, above which the excitation will exceed the damping. Furthermore it is clear that this whirl will not necessarily be synchronous. Future measurements using the internal balance will examine the hydrodynamic contribution to the damping and mass matrices; this will allow more quantitative analysis of hydrodynamically induced whirl.

Finally, we note that the force matrix data implies a "hydrodynamic center" within the volute; when the impeller center coincides with this "hydrodynamic center" the force $\{F_i\}$ is zero. The position of the "hydrodynamic center" for the Impeller X, Volute A is presented as a function of flow coefficient in Fig.11 where the origin is the center of the logarithmic spiral volute shape. It is seen that this data is consistent with that of Domm and Hergt (Ref.3) for a similar volute.

STATIC PRESSURE MEASUREMENTS IN THE VOLUTE

Typical static pressure distributions in the impeller discharge flow (measured as described earlier) are presented in Fig.12 for various flow coefficients and for seal clearances of 0.79mm. This data is for the impeller position labeled "closest" in Fig.4. The form and magnitude of the pressure variations are similar to those measured by Iversen et al (Ref.6) and to those predicted theoretically by Kurokawa (Ref.15). The pressure distributions were integrated numerically to obtain static pressure forces on the impeller for each of the four impeller positions indicated in Fig.14. Figure 13 presents the X and Y components of these static pressure forces for one of the four positions and compares them with the total force components on the impeller measured by the external balance for the same impeller location. Note that the static pressure component is not sufficient in itself to explain the measured total force. This is contrary to the result obtained by Iversen et al (Ref.6); they observed significant agreement between the forces. On the other hand we conclude that the discrepancy in the forces presented in Fig.13 is due to a difference in net flux of momentum into and out of the volute. Some measure of the order of magnitude of this momentum flux difference can be obtained by evaluation of the momentum flux discharging from the volute which, when non-dimensionalized in the same manner as the forces leads to a momentum flux in the Y direction of $4.14\varphi^2$. This is of the same order of magnitude as the forces. We conclude that the non-isotropy of the momentum is an important contribution to the impeller forces.

Results similar to Fig.13 were obtained for each of the four positions in Fig.4. Hence hydrodynamic force matrices or stiffness matrices due to the static pressure forces could be evaluated. It transpires that this component represents only about 20% of the magnitude of the total force matrices presented in Fig.10. We therefore conclude that the non-isotropy of the momentum flux is the primary contributor to the stiffness matrix. This fact emphasizes the need for direct measurement of the forces on the impeller.

CONCLUDING REMARKS

This paper has presented measurements of the hydrodynamic forces on a centrifugal pump impeller as a function of position within a logarithmic spiral volute. These correspond to the forces experienced by the impeller at zero whirl frequency. The hydrodynamic force matrices (negative of the hydrodynamic stiffness matrices) derived from these measurements exhibit both diagonal and off-diagonal terms of substantial magnitude. The off-diagonal or cross-coupling terms are of a form which would tend to excite a whirl motion in a rotordynamic analysis of the pump.

Static pressure measurements in the impeller discharge flow show that the hydrodynamic force on the impeller contains a substantial component due to the non-isotropy of the net momentum flux leaving the impeller. Moreover a similar breakdown of the contributions to the stiffness matrices reveals that the major component of these matrices results from the non-isotropy of the momentum flux.

Future plans include measurement of these forces at non-zero whirl frequencies in order to obtain a complete picture of the rotordynamic consequences of these hydrodynamic forces.

REFERENCES

1. Alford, J. S.: Protecting Turbmachinery from Self-excited Rotor Whirl. J. Eng. Power, vol. 87 A, 1965, pp. 333-344.

2. Thompson, W. E.: Fluid Dynamic Excitation of Centrifugal Compressor Rotor Vibrations. J. Fluid Engineering, vol. 100, no. 1, 1978, pp. 73-79.

3. Stepanoff, A. J.: Centrifugal and Axial Flow Pumps. Wiley, New York, 2nd Edition, 1957, pp. 116-123.

4. Domm, H.; and Hergt, P.: Radial Forces on Impeller of Volute Casing Pumps. Flow Research on Blading (L. S. Dzung, ed.), Elsevier, 1970, pp. 305-321.

5. Agostinelli, A.; Nobles, D.; and Mockridge, C. R.: An Experimental Investigation of Radial Thrust in Centrifugal Pumps. Trans, ASME, J. of Eng. for Power, 1960, pp. 120-126.

6. Iversen, H. W.; Rolling, R. E.; and Carlson, J. J.: Volute Pressure Distribution, Radial Force on the Impeller and Volute Mixing Losses of a Radial Flow Centrifugal Pump. Trans. ASME, J. of Eng. for Power, 1960, pp. 136-144.

7. Hergt, P.; and Krieger, P.: Radial Forces in Centrifugal Pumps with Guide Vanes. Proc. Inst. Mech. Engrs., vol. 184, Pt.3N, pp. 101-107, 1969-70.

8. Colding-Jorgensen, J.: The Effect of Fluid Forces on Rotor Stability of Centrifugal Compressors and Pumps. Ing. Thesis, Technical University of Denmark, 1979.

9. Chamieh, D.; and Acosta, A. J.: Dynamic Forces on a Whirling Centrifugal Rotor. Proc. 6th Conf. on Fluid Machinery, Akademiai Kiado, Budapest, Hungary, 1979, pp. 210-219.

10. Chamieh, D.: Calculation of the Stiffness Matrix of an Impeller Eccentrically Located within a Volute. Cavitation and Polyphase Flow Forum, Joint ASME - ASCE Solid and Fluid Mechanics Conference, Boulder, Colorado, pp. 51-53, 1981.

11. Imaichi, K.; Tsujimoto, Y.; and Yoshida, Y.: A Two Dimensional Analysis of the Interaction Effects of Radial Impeller in Volute Casing. IAHR/AIRH Symposium, Tokyo, Japan, 1980, pp. 635-647.

12. Shoji, H.; and Ohashi, H.: Fluid Forces on Rotating Centrifugal Impeller with Whirling Rotors. NASA Conf. Pub. 2133, Texas A & M University, College Station, Texas, 1980, pp. 317-328.

13. Brennen, C. E.; Acosta, A. J.; and Caughey, T. K.: A Test Program to Measure Fluid Mechanical Whirl-Excitation Forces in Centrifugal Pumps. NASA Conference Publication 2133, 1980, pp. 317-328.

14. Adams, M. L.; and Padovan, J.: Insights into Linearized Rotor Dynamics. Journal of Sound and Vibration, 1981, pp. 129-142.

15. Kurokawa, J.: Theoretical Determinations of the Flow Characteristics in Volutes. IAHR/AIRH Symposium, Tokyo, Japan, 1980, pp. 623-634.

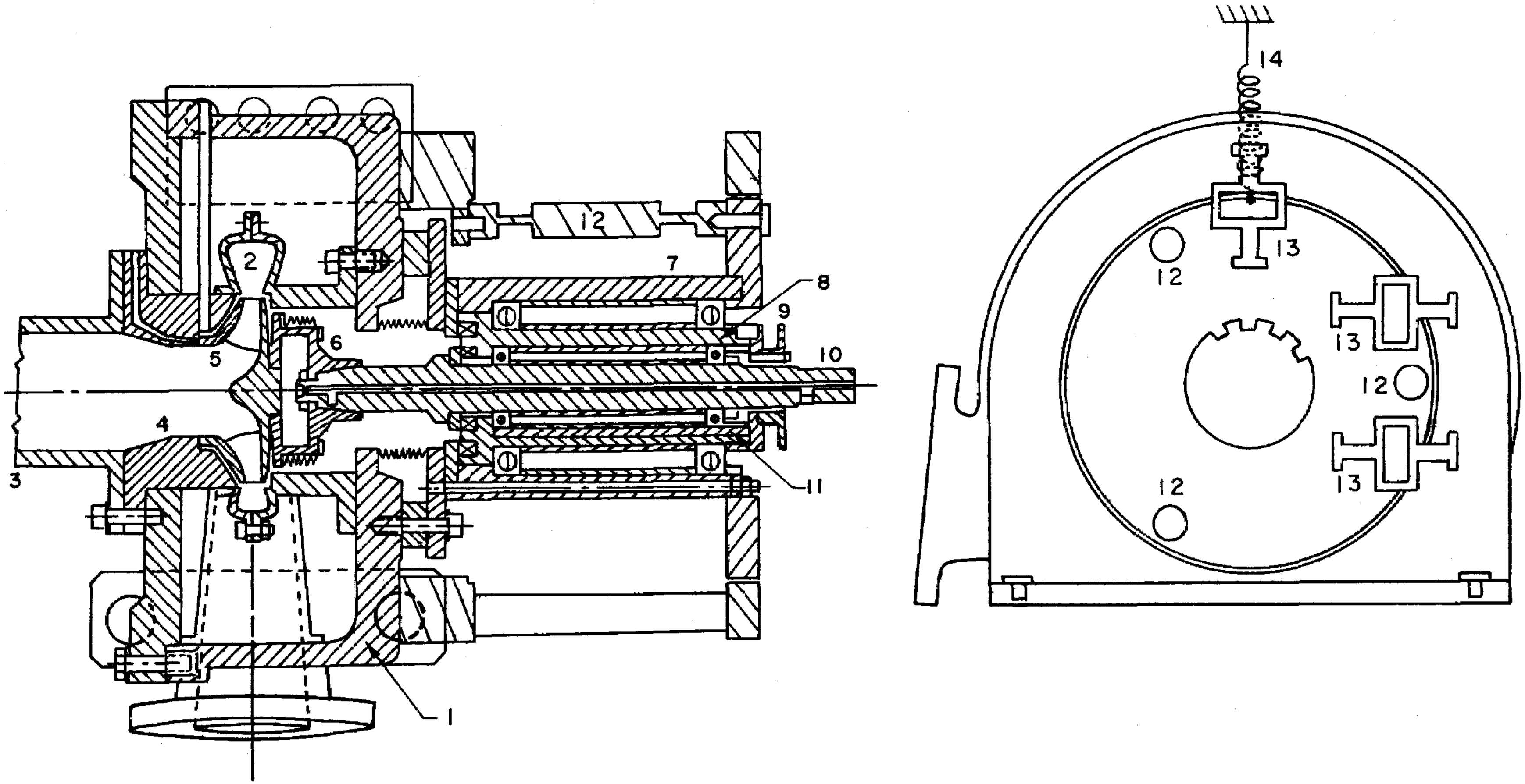

PLAN VIEW

ELEVATION VIEW

Figure 1. - Schematic of pump housing and force balance assembly of rotor test force test facility. Pump housing (1), volute (2), inlet connection (3), inlet bell (4), impeller (5), internal balance (6), double bearing system (7,8,11), orbiting motion sprocket (9), main shaft (10), axial retaining flexure (12), external balance flexure (13), retaining spring (14).

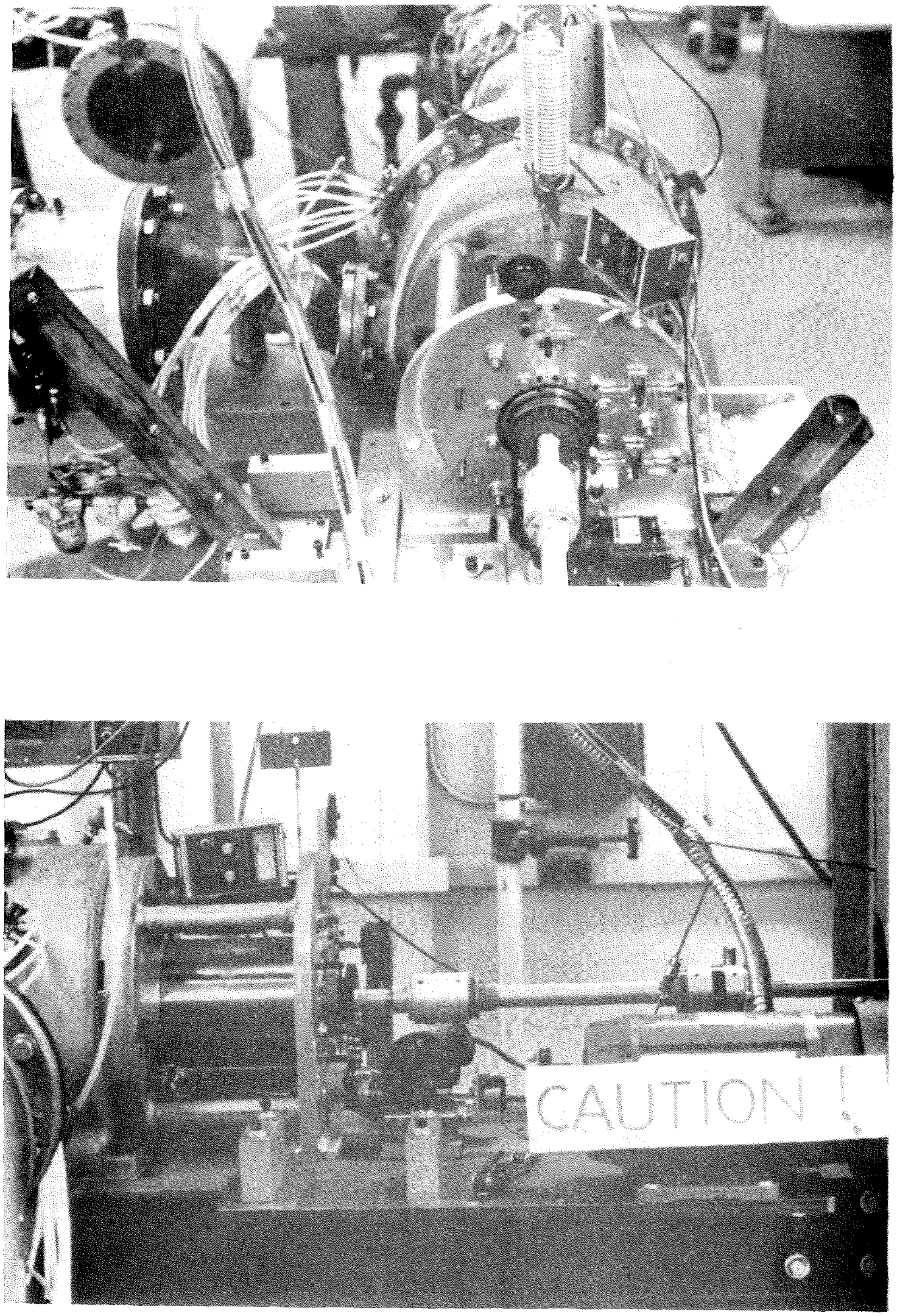

Figure 2. - Photographs of the items shown in Figure 1.

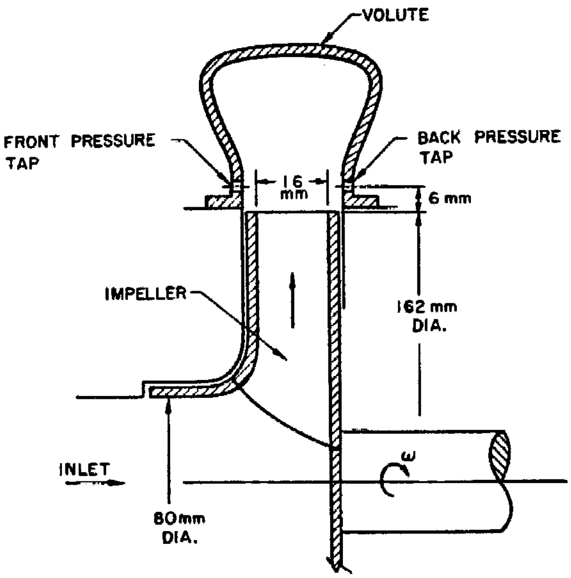

Figure 3. - Schematic showing main dimension and static pressure measurement points within volute. (Eight pressure taps more or less equally spaced around volute circumference on front and back.)

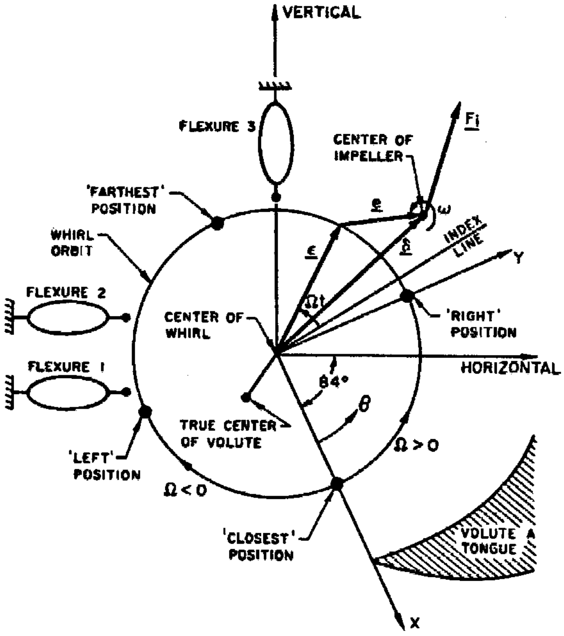

Figure 4. - Schematic of forces and locations within impeller-volute system as seen from inlet.

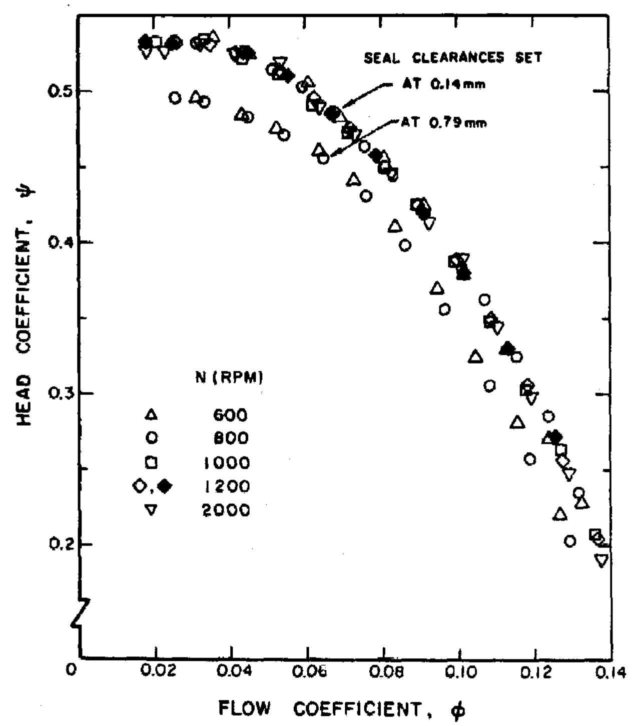

Figure 5. - Performance characteristic of Impeller X inside Volute A for front and back seal clearances of 0.14 and 0.79 mm. (Open and closed symbols represent data for $\Omega>0$ and $\Omega<0$ respectively.)

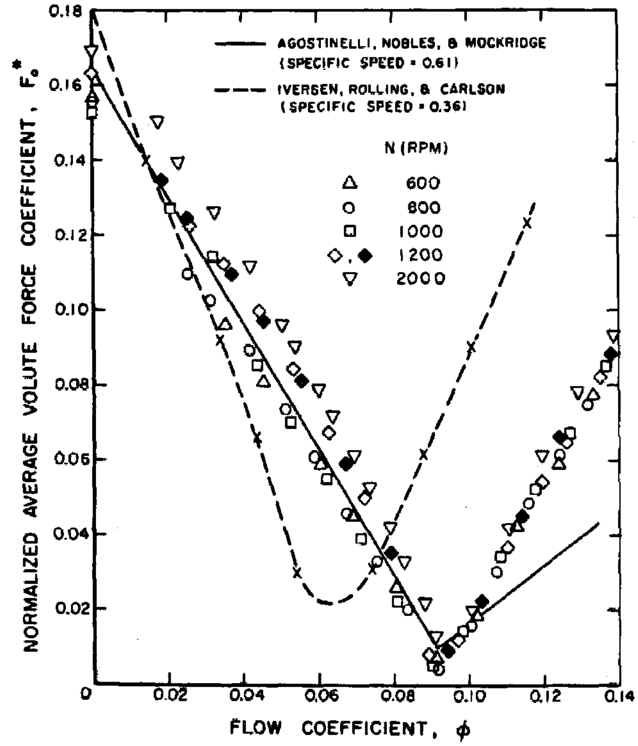

Figure 6. - Normalized average volute force for Impeller X, Volute A, and seal clearances of 0.14 mm. (Open and closed symbols represent data for $\Omega>0$ and $\Omega<0$, respectively. Comparison is made with Iversen et al. (ref.6) bearing reactions and Agostinelli et al. (ref.5) experimental data.)

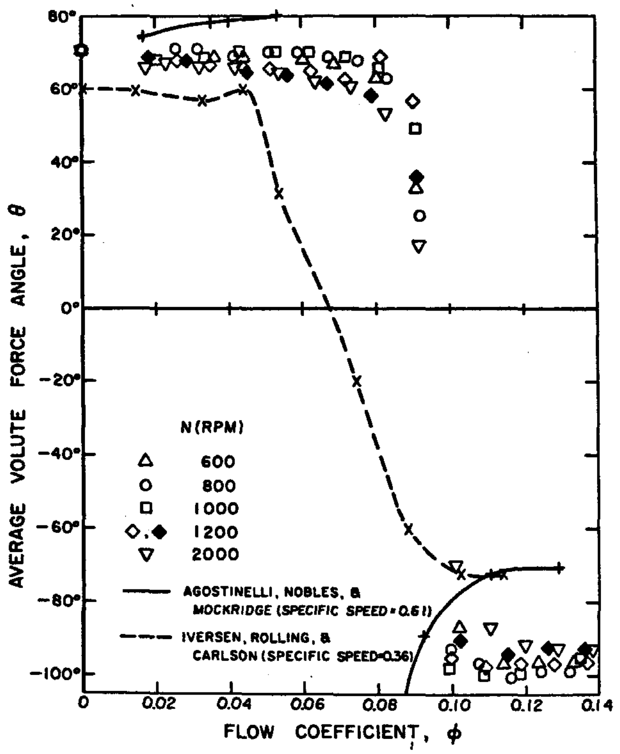

Figure 7. - Direction of average volute force plotted in figure 6 expressed in volute coordinate system. (θ is the angle between the direction of average force and line joining center to tongue of volute.)

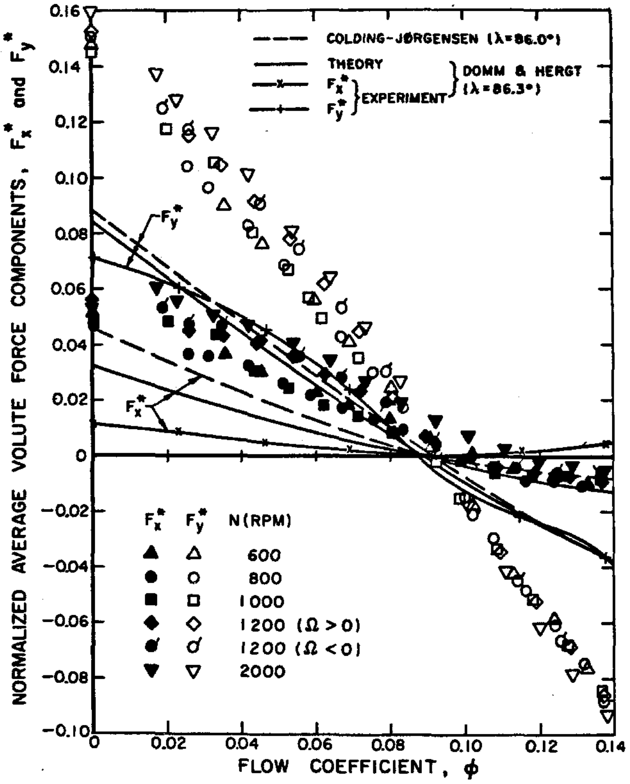

Figure 8. - Comparison of normalized average volute force components of figures 6 and 7 with work of Domm and Hergt (ref.4) and Colding-Jorgensen (ref.8). (Impeller X, Volute A, and seal clearances of 0.14 mm).

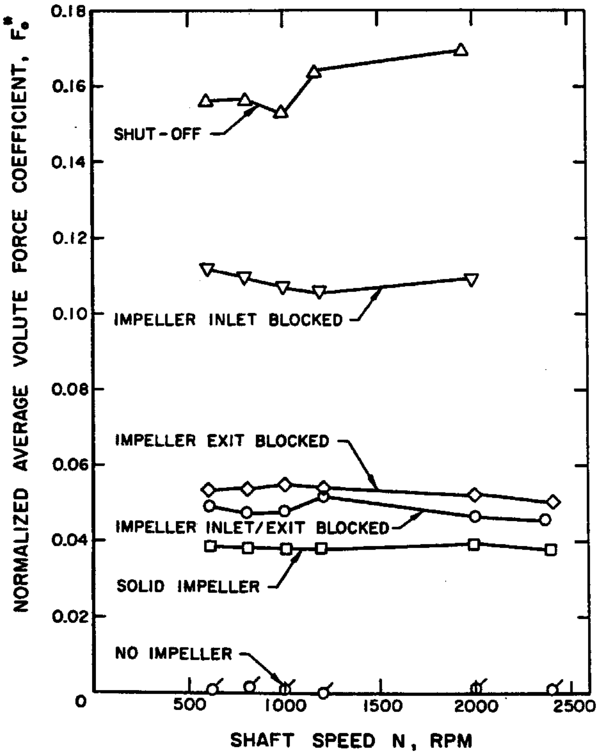

Figure 9. - Normalized average volute force as function of shaft speed for various auxiliary experiments. (Impeller X, Volute A, and seal clearances at 0.14 mm).

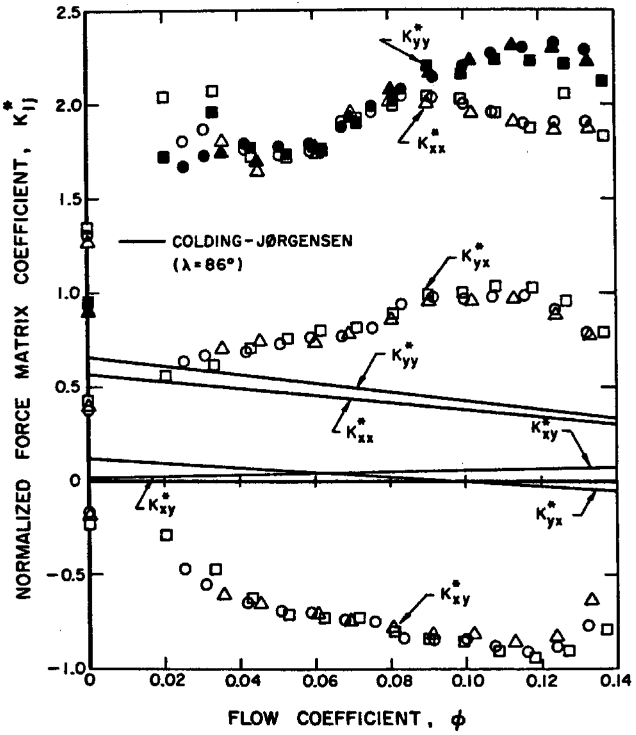

Figure 10. - Force matrix coefficients as defined in text (Impeller X, Volute A, and seal clearances at 0.14 mm), shaft speed = 600 rpm: △,▲; 800 rpm ○,●; 1000 rpm: □,■. (Values of K_{xx}^*, K_{xy}^*, and K_{yx}^* are represented by open symbols; values of K_{yy}^* by closed symbols.)

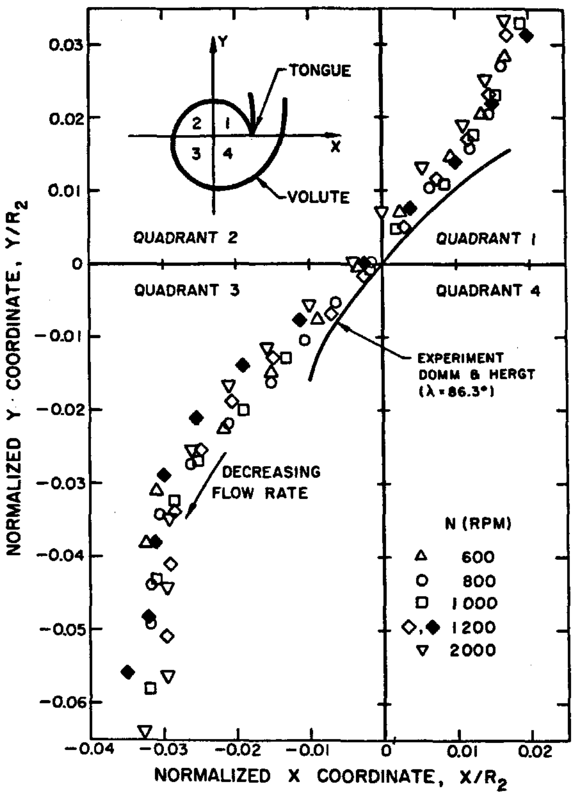

Figure 11. - Equilibrium positions of Impeller X within Volute A for seal clearances of 0.14 mm for various flow rates. Solid line indicates experimental data of Domm and Hergt (ref.4) for $\lambda = 86.3_0$.

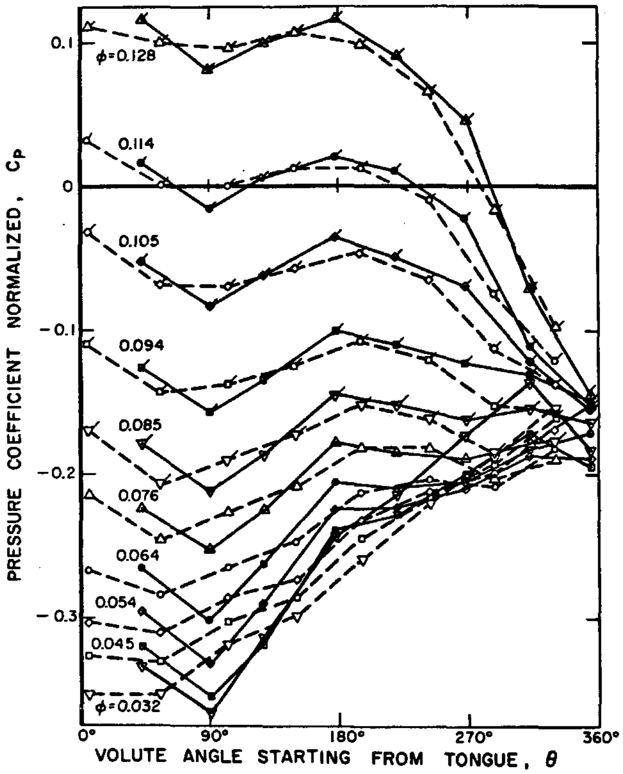

Figure 12. - Pressure coefficient for various flow rates for main shaft speed N = 600 rpm. Impeller X, Volute A, and seal clearances at 0.79 mm. Shaft center position is at 'closest' point (fig.4). Solid lines represent front pressure taps and dashed line back pressure taps of figure 3.

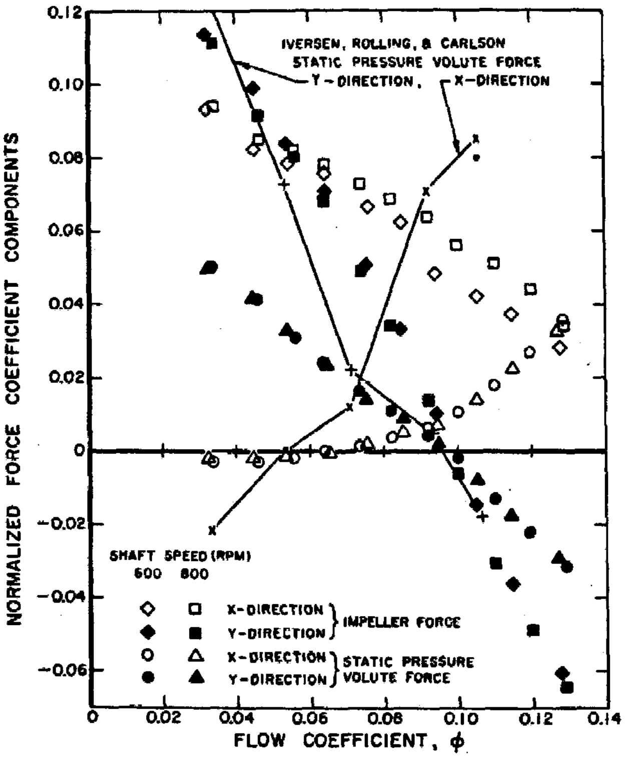

Figure 13. - Normalized impeller forces and static pressure forces of figure 12 shown for main shaft speed N = 600 rpm. Impeller X, Volute A, and seal clearances set at 0.79 mm. Shaft center position is at 'closest' point (fig.4). Comparison is made with Iversen et al. (ref.6) static pressure volute forces.